

# Polarimetric Scattering Spectrum Analysis for Target Characterization

Subhadip Dey, *Graduate Student Member, IEEE*, Noelia Romero-Puig, *Member, IEEE*,  
 Avik Bhattacharya, *Senior Member, IEEE*

**Abstract**—This study proposes the spectrum analysis of the scattering-type parameter,  $\theta_{FP}$ , to characterize different land cover targets. Many orthonormal projections of the scattering information onto distinct polarization bases have been proposed in the literature. However, these conventional orthonormal basis projection techniques often provide various target characterization ambiguities and classification. In this work, we propose projecting the target coherency matrix onto several random realizations of the normalized scattering configuration without restriction to the orthogonality constraint. This unique approach helps enhanced target characterization from polarimetric SAR data. We show the efficacy of our proposed technique over different land cover types using the C-band RADARSAT-2 data over SF and the L-band ALOS-2 data over Mumbai.

**Index Terms**—SAR, Scattering type parameter, Polarimetry, Spectrum analysis, Radar

## I. INTRODUCTION

In radar polarimetry, target characterization using an invariant descriptor is essential in identifying diverse land cover types. In this regard, one could characterize targets using: a coherent scattering matrix, the Stokes reflection or Muller matrix, and incoherent target coherency (or covariance) matrix [1]. Incoherent target characterization can be represented as the sum of the average scattering mechanisms from each independent target within a radar resolution cell. Huynen [2] introduced the phenomenological concept of radar target characterization.

Later, Cloude pointed out that the phenomenological theory does not provide global invariance if Huynen's restriction on roll-invariance is removed. Hence, Cloude and Pottier proposed an eigen-decomposition based scattering-type parameter in the linear H–V basis to overcome the parameter proliferation problem [1]. Since then, this eigen-decomposition technique has been the most used approach for characterizing natural target scattering. The characteristic decomposition of the coherency matrix (in linear H–V basis) produces a scattering-type parameter,  $\bar{\alpha}$ .

Although the scattering-type parameter  $\bar{\alpha}$  is effective in characterizing diverse targets, it remains ambiguous between a helix and a dihedral target. Hence, Corr and Rodrigues [3] projected the scattering information onto another orthonormal

basis composed of a sphere and a pair of left- and right-handed helices, thereby resolving the scattering ambiguity.

Furthermore, concerning the ambiguities of  $\bar{\alpha}$  and the issues presented in [3], Touzi [4] proposed a new scattering vector model by projecting the Kennaugh-Huynen scattering matrix condiagonalization into the Pauli basis. This unique proposal provided a complete polarization basis invariant scattering-type parameter,  $\alpha_s$ .

Recently, Dey et al. [5], [6] proposed a new target characterization parameter,  $\theta_{FP}$  in the linear H–V basis. Nonetheless,  $\theta_{FP}$  also remains ambiguous in characterizing the helix and the dihedral targets.

Overall, one can witness from the literature that projecting the scattering information onto a specific orthonormal basis could resolve certain issues of target characterization ambiguities. Nevertheless, certain other types of ambiguities can emerge for target characterization. Therefore, there is a need to assess the entire spectrum (i.e., all possible values) of  $\theta_{FP}$ , obtained by randomly varying the scattering bases. The number of elements in any orthonormal basis is restricted by the dimension of the incoherent scattering covariance matrix. Hence, using only those bases, it might not be possible to characterize the complete set of scattering mechanisms of a target in a radar resolution cell.

This study proposes the spectrum analysis of  $\theta_{FP}$  by projecting the incoherent coherency matrix onto different scattering mechanism bases. This projection essentially produces complete information about the target within the whole scattering spectrum. We further utilize the spectrum of  $\theta_{FP}$  to classify important land cover types over two different SAR images of C- and L-bands, respectively.

## II. METHODOLOGY

### A. The Scattering-Type Parameter

In full-polarimetric (FP) SAR, the  $2 \times 2$  complex scattering matrix  $\mathbf{S}$  encompasses complete polarimetric information about backscattering from targets for each pixel. It is expressed in the backscatter alignment (BSA) convention in the linear horizontal (H) and linear vertical (V) polarization basis as,

$$\mathbf{S} = \begin{bmatrix} S_{HH} & S_{HV} \\ S_{VH} & S_{VV} \end{bmatrix} \Rightarrow \vec{k} = V([\mathbf{S}]) = \frac{1}{2} \text{Tr}(\mathbf{S}\Psi) \quad (1)$$

where  $V(\cdot)$  is the vectorization operator on the scattering matrix,  $\Psi$  are the corresponding Pauli basis matrices, and  $\text{Tr}$  is the sum of the diagonal elements of the matrix. The second-order scattering information in terms of the  $3 \times 3$  coherency

S. Dey and N. Romero-Puig are with the Microwaves and Radar Institute, German Aerospace Centre (DLR), Germany, (e-mail: sdey2307@gmail.com; noelia.romerpuig@dlr.de).

A. Bhattacharya is with the Microwave Remote Sensing Lab, Center of Studies in Resources Engineering, Indian Institute of Technology Bombay, India, (e-mail: avikb@csre.iitb.ac.in).

The authors thank MAXAR Technologies Ltd. for the RADARSAT-2 data, and JAXA for the ALOS-2 PALSAR data.

matrix  $\mathbf{T}$ , can be obtained as the ensemble average  $\langle \cdot \rangle$  of the outer product of the scattering vector  $\vec{k}$  with its conjugate transpose  $\vec{k}^{*T}$  as  $\mathbf{T} = \langle \vec{k} \vec{k}^{*T} \rangle$ , which in general is a rank-3 matrix.

Next, let us define an arbitrary  $3 \times 1$  complex vector  $\vec{\omega}$  as,

$$\vec{\omega} = \begin{bmatrix} Ae^{i\phi_1} \\ Be^{i\phi_2} \\ Ce^{i\phi_3} \end{bmatrix} \quad (2)$$

where,  $A$ ,  $B$  and  $C$  are the magnitudes of each component and  $\phi_1$ ,  $\phi_2$  and  $\phi_3$  are their phases, respectively. We then project the normalized complex vector  $\vec{\omega}_n = \vec{\omega}/|\vec{\omega}|$  by the coherency matrix  $\mathbf{T}$  as,

$$\vec{\omega}_s = \mathbf{T}\vec{\omega}_n. \quad (3)$$

Thus,  $\vec{\omega}_s$  allows us to project the data (i.e.,  $\mathbf{T}$ ), onto any arbitrary scattering basis (by varying  $\vec{\omega}_n$ ). Since  $\mathbf{T}$  is positive semi-definite,  $\langle \vec{\omega}_n^* \vec{\omega}_s \rangle \geq 0$ . This intuitively also suggests that  $\vec{\omega}_s$ , in general, points to the same direction as  $\vec{\omega}_n$  (i.e., the angle between  $\vec{\omega}_n$  and  $\vec{\omega}_s$  is less than  $\pi/2$ ). One can note that  $\vec{\omega}_s = \vec{\omega}_n$  only when  $\mathbf{T}$  represents the coherency matrix of a canonical target (e.g., dihedral, trihedral, helix, etc.) or any rank-1 matrix.

We utilize this projected vector  $\vec{\omega}_s$  to obtain a rank-1 higher-order coherency matrix,  $\mathbf{T}_s$ , as the ensemble average of the outer product of the projected vector  $\vec{\omega}_s$  with its conjugate transpose  $\vec{\omega}_s^{*T}$ ,

$$\mathbf{T}_s = \langle \vec{\omega}_s \vec{\omega}_s^{*T} \rangle \quad (4)$$

where  $\mathbf{T}_s$  is Hermitian and positive semi-definite. Since  $\mathbf{T}_s$  contains higher-order covariance information, we convert it to a second-order covariance structure using the following theorem.

*Theorem 1:* Let  $\mathbf{A}$  be a positive semi-definite matrix (real or complex). Then, there is exactly one positive semi-definite (and hence symmetric) matrix  $\mathbf{B}$  such that  $\mathbf{A} = \mathbf{B}^* \mathbf{B}$ .

Therefore, using the above theorem we can express  $\mathbf{T}_s = \mathbf{T}_p^* \mathbf{T}_p$ . The Schur factorization method is used to compute the matrix square root. The matrix  $\mathbf{T}_p$  is unique and is called the principal square root matrix. Moreover, since  $\mathbf{T}$  is defined as the outer product of the scattering vector represented in the Pauli matrix basis, one can inherently relate  $\mathbf{T}_p$  to a canonical target representation on the same basis. Therefore,  $\mathbf{T}_p$  can be utilized to characterize different physical properties of targets.

We then derive the scattering-type parameter,  $\theta_{\text{FP}}^p$  from the elements of  $\mathbf{T}_p$  as proposed by Dey et al., [5] as,

$$\tan \theta_{\text{FP}}^p = \frac{m_{\text{FP}} \text{Span} (T_{11} - T_{22} - T_{33})}{T_{11} (T_{22} + T_{33}) + m_{\text{FP}}^2 \text{Span}^2} \quad (5)$$

where,  $m_{\text{FP}}$  is the 3D Barakat degree of polarization [7] and  $T_{11}$ ,  $T_{22}$  and  $T_{33}$  are the diagonal elements of  $\mathbf{T}_p$  with  $\text{Span} = T_{11} + T_{22} + T_{33}$ .

Similar to the conventional degree of polarization  $m$ , the 3D Barakat degree of polarization  $m_{\text{FP}}$  also characterizes the state of polarization (or purity) of an EM wave. For a completely polarized EM wave,  $m = 1$  and for a completely unpolarized EM wave,  $m = 0$ . The EM wave is said to be partially polarized between these two extreme cases,  $0 < m < 1$ .

However, one can note that for  $\mathbf{T}_p$ , which is a rank-1 matrix,  $m_{\text{FP}} = 1$ .

$\theta_{\text{FP}}^p$  varies within the range:  $[-45^\circ, 45^\circ]$ . For a pure dihedral target,  $\theta_{\text{FP}}^p = -45^\circ$ , and for a pure trihedral target,  $\theta_{\text{FP}}^p = 45^\circ$ . We generate the spectrum of  $\theta_{\text{FP}}^p$  by arbitrarily varying  $\vec{\omega}_n$ . Each realization of  $\vec{\omega}_n$  can be considered as a representative scattering mechanism.

In the following section, we demonstrate the characteristics of the  $\theta_{\text{FP}}^p$  spectrum over different standard coherent and incoherent targets.

## B. Analysis over Different Scatterers

The histogram of the spectrum of  $\theta_{\text{FP}}^p$  for different targets is shown in Fig. 1. It includes different coherent (viz., trihedral and dihedral) and incoherent (viz., random volume [8] and volume of horizontal dipole [9]) targets, as well as different land cover targets, such as waterbodies, urban, oriented urban, and vegetation.

To generate the histograms of  $\theta_{\text{FP}}^p$ , we have considered 1000 realizations of the normalized scattering configuration,  $\vec{\omega}_n$ . We then computed the median value of  $\theta_{\text{FP}}^p$  as the mean over 20 iterations. We have also compared the values of the Cloude average scattering-type parameter  $\bar{\alpha}$  [1]. However, to provide its interpretation similar to  $\theta_{\text{FP}}$ , we express  $\hat{\alpha} = 45^\circ - \bar{\alpha}$  (i.e.,  $\hat{\alpha} \in [-45^\circ, 45^\circ]$ ).

It can be seen from Fig. 1a and Fig. 1b that the distribution of the spectrum of  $\theta_{\text{FP}}^p$  represents a Dirac-delta function at  $45^\circ$  and  $-45^\circ$ , corresponding to the trihedral (odd-bounce) and dihedral (even-bounce) targets, respectively.

Incoherent targets, i.e., random volume in Fig. 1c and volume of horizontal dipoles in Fig. 1d, exhibit the existence of all  $\theta_{\text{FP}}^p$  values in the spectrum. In both cases, the median value of the  $\theta_{\text{FP}}^p$  spectrum lies around  $4^\circ$ , whereas  $\hat{\alpha}$  varies around  $0^\circ$ . Thus, the median values indicate a certain amount of regular scattering mechanisms from the volume targets.

Over the land cover targets, i.e., waterbody, urban, oriented urban, and vegetation, we observe distinct histograms of the  $\theta_{\text{FP}}^p$  spectrum. Over the waterbody, the median value of  $\theta_{\text{FP}}^p$  is  $43.49^\circ \pm 0.04^\circ$ , while  $\hat{\alpha} \approx 35^\circ$ . This high median value is due to the dominating odd-bounce scattering mechanism. Generally, when the ocean surface is smooth, co-polarized backscatter signatures show a low coefficient of variation. As a result, the width of the histogram is small over such a target.

Over the urban target, we observe that the median value of  $\theta_{\text{FP}}^p$  is  $-27.24^\circ \pm 0.72^\circ$ , whereas  $\hat{\alpha} \approx -15^\circ$ . Besides, the histogram of the spectrum of  $\theta_{\text{FP}}^p$  is right-tailed. This indicates the presence of a small orientation of the urban target to the radar line of sight. Moreover, the  $\theta_{\text{FP}}^p$  values indicate the presence of the even-bounce scattering characteristics of the target. An interesting shift in the median value, as well as in the characteristics of the histogram, can be seen over the obliquely oriented urban targets in Fig. 1g. This orientation contributes to a strong cross-polarization component [10] which, in turn, reduces the median value of the spectrum to  $-14.03^\circ \pm 0.41^\circ$ . In this case,  $\hat{\alpha} \approx -6^\circ$ . Primarily, one can note that for both urban and oriented urban targets, the standard deviations of the spectrum increase with respect to the waterbody case.

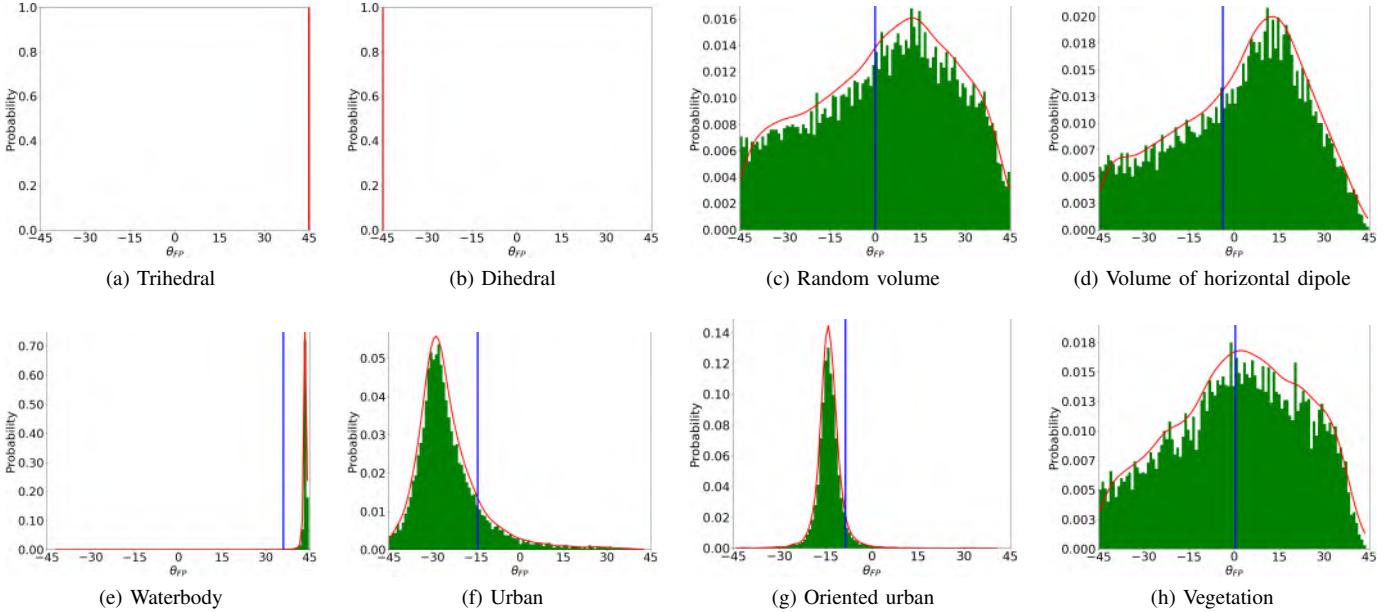


Fig. 1: Histogram of  $\theta_{FP}^p$  (in degrees) for different canonical targets: (a) Trihedral, and (b) Dihedral, different volume targets: (c) Random volume, (d) Horizontal oriented volume, and different land cover targets: (e) Waterbody, (f) Urban, (g) Oriented urban, and (h) Vegetation using full-pol RADARSAT-2 C-band data. The red bounding curve represents the kernel-density estimate using the Gaussian kernels. The vertical blue line represents  $\hat{\alpha} = 45^\circ - \bar{\alpha}$  value.

Over the vegetation target, we observe similar characteristics as those in the random volume and volume of the horizontal dipole. The median value of the histogram of the  $\theta_{FP}$  spectrum is  $2.4^\circ \pm 0.32^\circ$ , and  $\hat{\alpha}$  is centered around  $0^\circ$ .

### III. RESULTS AND DISCUSSION

We used two FP SAR images over San Francisco (SF), USA, and Mumbai, India, as shown in Fig. 2a and Fig. 5a, respectively. The C-band RS-2 SF scene has near- and far-range incidence angles of  $28.02^\circ$  and  $29.81^\circ$ , respectively. The single look complex (SLC) image is multilooked by a factor of 2 in the range direction and 4 in the azimuth direction to generate a  $20\text{ m}^2$  ground pixel. The L-band ALOS-2 Mumbai scene has a center incidence angle of  $33^\circ$ , as shown in Fig. 5a. The image is multilooked by a factor of 3 in the range direction and 5 in the azimuth direction to generate  $15\text{ m}^2$  pixels.

For both images, the ground truth data is generated using Google Earth images, as shown in Fig. 2a and Fig. 5a, respectively. Here, we have used the K-means unsupervised clustering algorithm with three classes, as represented in Fig. 2b and Fig. 5b: urban areas in red, vegetation in green, and waterbody in blue. We have compared the clustering results between  $(\theta_{FP}^{(1)}, \theta_{FP}^{(2)}, \theta_{FP}^{(3)})$  and the  $\theta_{FP}$  spectrum.  $(\theta_{FP}^{(1)}, \theta_{FP}^{(2)}, \theta_{FP}^{(3)})$  are the three scattering mechanisms obtained from the elements of the three rank-1 coherency matrices corresponding to the three orthogonal eigen-polarization states obtained from the eigen-decomposition of the  $\mathbf{T}$  matrix. We generated 100 random realizations of  $\theta_{FP}^p$  for the classification purpose.

The unsupervised classification maps over the SF area using RADARSAT-2 data are shown in Fig. 4. We have considered three main land cover types, i.e., urban, vegetation

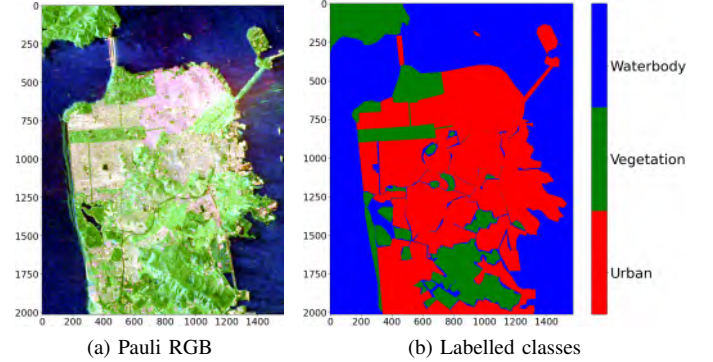


Fig. 2: RADARSAT-2 SAR data over the SF area. (a) Pauli RGB. (b) Labelled classes.

and waterbody, defined in Fig. 2b. The median values of different target scattering type parameters are computed using randomly selected pixels from each land cover target. Over the waterbody, we observe the median value of  $\theta_{FP}^p$  is, approximately,  $41^\circ \pm 0.2^\circ$ , while the median value of  $\theta_{FP}^{(1)} \approx 43^\circ$ , and the median values of  $\theta_{FP}^{(2)}$  and  $\theta_{FP}^{(3)}$  are both around  $-37^\circ$ .

Over the urban region, we observe a median value of  $\theta_{FP}^p \approx -22^\circ \pm 2.1^\circ$ . The median value of  $\theta_{FP}^{(1)}$  ranges from around  $-28^\circ$  to  $-37^\circ$ , and the median values of  $\theta_{FP}^{(2)}$  and  $\theta_{FP}^{(3)}$  are around  $-4^\circ$  to  $36^\circ$ . These values of the scattering-type parameters characterize urban targets (corresponding to dihedral scatterers).

Similarly, over the vegetation region, the median value of  $\theta_{FP}^p \approx 4.3^\circ \pm 1.4^\circ$ . The median value of  $\theta_{FP}^{(1)}$  ranges from  $12^\circ$

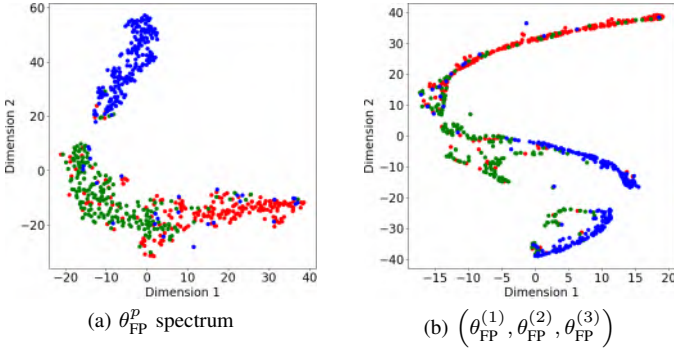


Fig. 3: t-SNE plot for (a)  $\theta_{FP}^p$  spectrum and (b)  $(\theta_{FP}^{(1)}, \theta_{FP}^{(2)}, \theta_{FP}^{(3)})$  correspond to the RADARSAT-2 data over SF. Points in Red: urban, Green: vegetation, Blue: waterbody.

to  $30^\circ$ , approximately, and the mean values of  $\theta_{FP}^{(2)}$  and  $\theta_{FP}^{(3)}$  are around  $2^\circ$  to  $-29^\circ$ . Therefore, a similarity in the  $\theta_{FP}^{(1)}$ ,  $\theta_{FP}^{(2)}$  and  $\theta_{FP}^{(3)}$  values can be noticed among these three land cover types. Hence, to evaluate the efficacy of the  $\theta_{FP}^p$  spectrum over  $\theta_{FP}^{(1)}$ ,  $\theta_{FP}^{(2)}$  and  $\theta_{FP}^{(3)}$ , quantitative accuracy results are shown in Table I and Table II, respectively.

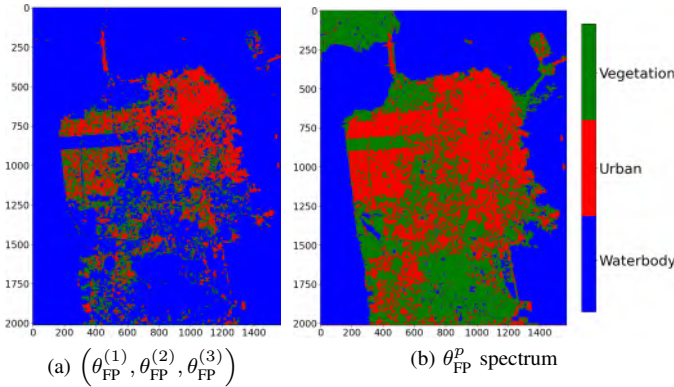


Fig. 4: Unsupervised classified maps using the K-means classifier with (a)  $(\theta_{FP}^{(1)}, \theta_{FP}^{(2)}, \theta_{FP}^{(3)})$  and (b)  $\theta_{FP}^p$  spectrum for the RADARSAT-2 SAR data over SF.

From Table I and Table II, it can be seen that the overall accuracy using  $\theta_{FP}^{(1)}$ ,  $\theta_{FP}^{(2)}$  and  $\theta_{FP}^{(3)}$  is 56.60%, while using the  $\theta_{FP}^p$  spectrum it is 77.49%. This means that an increase of around 20% overall classification accuracy is observed when using the  $\theta_{FP}^p$  spectrum. Moreover, very low User's Accuracy

TABLE I: Accuracy scores over different land cover targets using  $(\theta_{FP}^{(1)}, \theta_{FP}^{(2)}, \theta_{FP}^{(3)})$  for the RADARSAT-2 data over SF.

	Urban	Vegetation	Waterbody	Overall accuracy	Kappa score
UA	30.19%	5.84%	95.39%	56.60%	0.31
PA	91.31%	5.71%	61.03%		

(UA) and Producer's Accuracy (PA) are observed over the vegetation area using  $(\theta_{FP}^{(1)}, \theta_{FP}^{(2)}, \theta_{FP}^{(3)})$ . These low UA and PA are primarily due to the confusion between vegetation and

waterbody targets. This confusion can also be seen from the t-distributed Stochastic Neighbor Embedding (t-SNE) plot [11] in Fig. 3. It can be observed that distinct clusters exist for waterbody, vegetation and urban areas using the  $\theta_{FP}^p$  spectrum, while such clusters are not as prominent in the case of  $(\theta_{FP}^{(1)}, \theta_{FP}^{(2)}, \theta_{FP}^{(3)})$ .

TABLE II: Accuracy scores over different land cover targets using the  $\theta_{FP}^p$  spectrum for the RADARSAT-2 data over SF.

	Urban	Vegetation	Waterbody	Overall accuracy	Kappa score
UA	62.72%	86.23%	88.61%	77.49%	0.66
PA	87.48%	42.34%	98.19%		

One can also find similar results over the Mumbai region using ALOS-2 data. However, a slight variation in the targets response is observed according to the L-band wavelength when exploiting these data.

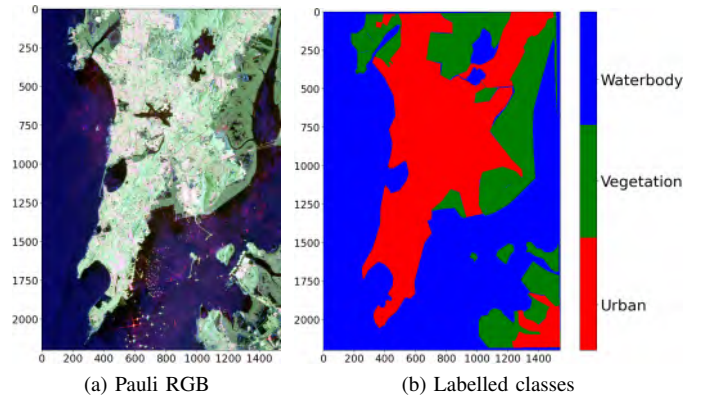


Fig. 5: ALOS-2 SAR data over the Mumbai area. (a) Pauli RGB. (b) Labelled classes.

In particular, for L-band ALOS-2 data we observe that the median value of the  $\theta_{FP}^p$  spectrum is  $37^\circ \pm 1.01^\circ$ . This low median value, as compared to that of RADARSAT-2 data, is due to the different interaction of the longer L-band wavelength with respect to the C-band wavelength. In addition, the existence of the mangrove region within the coastal extent increases the standard deviation of the  $\theta_{FP}^p$  spectrum. We observe a similar decrease of  $6^\circ$  in the median  $\theta_{FP}^{(1)}$  value over the waterbody. On the other hand, median values of  $\theta_{FP}^{(2)}$  and  $\theta_{FP}^{(3)}$  vary from  $2^\circ$  to  $-41^\circ$ .

Over the urban area, we observe a drastic decrease in the median value of the  $\theta_{FP}^p$  spectrum. The median value decreases by  $8^\circ$  compared to the urban area in the RADARSAT-2 data. Alongside this, the standard deviation of the  $\theta_{FP}^p$  spectrum also increases by  $2^\circ$ . This anomaly in the values of the  $\theta_{FP}^p$  spectrum is due to the existence of differently oriented urban areas within the scene. In this context, less urban density falls under the orthogonal urban area to the radar line of sight category. On the contrary, some very high  $\theta_{FP}^p$  values are outliers due to several ships in the ocean.

Similar characteristics are seen over the vegetation surface for both ALOS-2 and RADARSAT-2 data. The median value of the  $\theta_{FP}^p$  spectrum is around  $2.3^\circ \pm 2.4^\circ$ . The median value

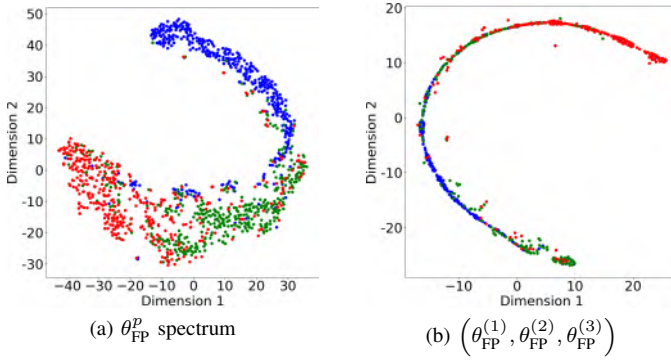


Fig. 6: t-SNE plot for (a)  $\theta_{FP}^p$  spectrum and (b)  $(\theta_{FP}^{(1)}, \theta_{FP}^{(2)}, \theta_{FP}^{(3)})$  correspond to the ALOS-2 data over Mumbai. Points in Red: urban, Green: vegetation, Blue: waterbody.

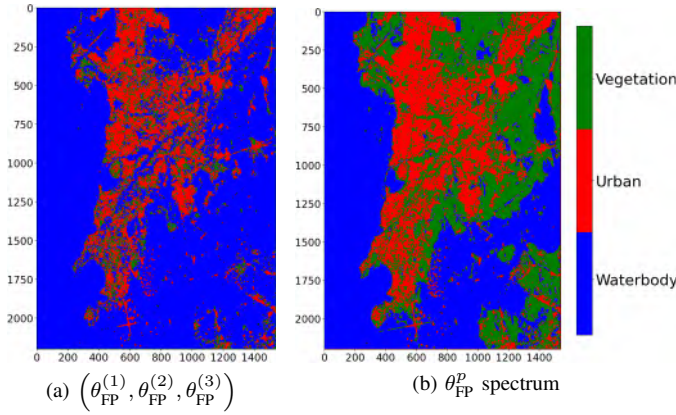


Fig. 7: Unsupervised classified maps using K-means classifier with (a)  $(\theta_{FP}^{(1)}, \theta_{FP}^{(2)}, \theta_{FP}^{(3)})$  and (b)  $\theta_{FP}^p$  spectrum for the ALOS-2 SAR data over Mumbai.

of  $\theta_{FP}^{(1)}$  ranges from  $-6^\circ$  to  $32^\circ$ , and the median values of  $\theta_{FP}^{(2)}$  and  $\theta_{FP}^{(3)}$  are around  $-14^\circ$  to  $-24^\circ$ , respectively. A slightly high mixed dihedral component is observed from the vegetation, possibly due to the subsurface canopy and underneath waterbody interaction of the SAR waves in the mangrove region.

TABLE III: Accuracy scores over different land cover targets using  $(\theta_{FP}^{(1)}, \theta_{FP}^{(2)}, \theta_{FP}^{(3)})$  for the ALOS-2 data over Mumbai.

	Urban	Vegetation	Waterbody	Overall accuracy	Kappa score
UA	81.18%	14.36%	65.01%	62.20%	0.32
PA	43.49%	8.31%	92.26%		

TABLE IV: Accuracy scores over different land cover targets using the  $\theta_{FP}^p$  spectrum for the ALOS-2 data over Mumbai.

	Urban	Vegetation	Waterbody	Overall accuracy	Kappa score
UA	79.60%	45.20%	92.03%	74.47%	0.60
PA	64.09%	76.46%	79.78%		

Accuracy classification results exploiting ALOS-2 data are shown in Table III and Table IV. The overall classification

accuracy is around 12% higher for the  $\theta_{FP}^p$  spectrum than when using  $(\theta_{FP}^{(1)}, \theta_{FP}^{(2)}, \theta_{FP}^{(3)})$ . Similar to the RADARSAT-2 data, a high confusion between vegetation and waterbody is observed. However, the UA and PA over the vegetation targets using  $(\theta_{FP}^{(1)}, \theta_{FP}^{(2)}, \theta_{FP}^{(3)})$  are slightly higher than in the SF image. This situation might be due to the enhanced information about the urban characteristics using the L-band SAR thanks to a larger penetration depth than at C-band. Nevertheless, the overall accuracy of the  $\theta_{FP}^p$  spectrum using L-band data decreases by 3% as compared to the C-band data. One can intuitively perceive this decrease in the overall classification accuracy from the t-SNE plot in Fig. 6. Interestingly, the vegetation and urban clusters in Fig. 6a are more mixed with the ocean cluster than in Fig. 3a.

#### IV. CONCLUSION

We propose a spectrum analysis of the target scattering type parameter  $\theta_{FP}$  by projecting the coherency matrix onto different non-orthogonal scattering mechanism bases. This information essentially helps us distinguish among different scattering targets by exploiting only one particular type of physical parameter instead of using several statistical and physical parameters, i.e.,  $\bar{\alpha}$  and entropy. We have shown the efficacy of the  $\theta_{FP}^p$  spectrum by comparing the target classification accuracy over different land cover types with scattering mechanisms at different eigen-polarization states,  $(\theta_{FP}^{(1)}, \theta_{FP}^{(2)}, \theta_{FP}^{(3)})$ . The classification results for the  $\theta_{FP}^p$  spectrum outperforms those with  $(\theta_{FP}^{(1)}, \theta_{FP}^{(2)}, \theta_{FP}^{(3)})$ . One can utilize this technique in several applications, like soil moisture retrieval, ship detection, and agricultural crop monitoring.

#### REFERENCES

- [1] S. Cloude, *Polarisation: applications in remote sensing*. OUP Oxford, 2009.
- [2] J. R. Huynen, "Phenomenological theory of radar targets," PhD dissertation, Technical Univ., Delf, The Netherlands, 1970.
- [3] D. Corr and A. Rodrigues, "Alternative basis matrices for polarimetric decomposition," in *Proc. Eusar*, 2002, pp. 597–600.
- [4] R. Touzi, "Target scattering decomposition in terms of roll-invariant target parameters," *IEEE Trans. Geosci. Remote Sens.*, vol. 45, no. 1, pp. 73–84, 2006.
- [5] S. Dey, A. Bhattacharya, D. Ratha, D. Mandal, and A. C. Frery, "Target characterization and scattering power decomposition for full and compact polarimetric SAR data," *IEEE Trans. Geosci. Remote Sens.*, vol. 59, no. 5, pp. 3981–3998, 2021.
- [6] S. Dey, A. Bhattacharya, A. C. Frery, C. López-Martínez, and Y. S. Rao, "A model-free four component scattering power decomposition for polarimetric SAR data," *IEEE J. Sel. Top. Appl. Earth. Obs. Remote Sens.*, vol. 14, pp. 3887–3902, 2021.
- [7] R. Barakat, "Degree of polarization and the principal idempotents of the coherency matrix," *Opt. Commun.*, vol. 23, no. 2, pp. 147–150, 1977.
- [8] A. Freeman and S. L. Durden, "A three-component scattering model for polarimetric SAR data," *IEEE Trans. Geosci. Remote Sens.*, vol. 36, no. 3, pp. 963–973, 1998.
- [9] Y. Yamaguchi, T. Moriyama, M. Ishido, and H. Yamada, "Four-component scattering model for polarimetric SAR image decomposition," *IEEE Trans. Geosci. Remote Sens.*, vol. 43, no. 8, pp. 1699–1706, 2005.
- [10] T. Ainsworth, D. Schuler, and J.-S. Lee, "Polarimetric SAR characterization of man-made structures in urban areas using normalized circular-polar correlation coefficients," *Remote Sens. Environ.*, vol. 112, no. 6, pp. 2876–2885, 2008.
- [11] L. Van der Maaten and G. Hinton, "Visualizing data using t-SNE." *J. Mach. Learn. Res.*, vol. 9, no. 11, 2008.